Thermodynamic and kinetic stability of Cl and F donors in ZnO

Supparat Charoenphon,[1] Audomsak Sripothongnack,[1] Sukit Limpijumnong,[2] and Pakpoom Reunchan[1,*]
[1]*Department of Physics, Faculty of Science, Kasetsart University, 50 Ngam Wong Wan Road, Lat Yao, Chatuchak, Bangkok 10900, Thailand*
[2]*National Science and Technology Development Agency (NSTDA) 111 Thailand Science Park, Phahonyothin Road, Khlong Nueng, Khlong Luang, Pathum Thani 12120, Thailand*

(Received 14 April 2026; accepted 31 July 2026; published 27 August 2026)

Zinc oxide (ZnO) is a prototypical wide-band-gap semiconductor whose *n*-type conductivity can be tailored through extrinsic donor doping. However, the roles of defect association, compensation, and dopant mobility remain incompletely understood. We investigate Cl- and F-related defects in ZnO using screened hybrid density-functional calculations, with emphasis on substitutional donors, defect complexes, vacancy-mediated migration, and self-consistent carrier statistics. Substitutional chlorine and fluorine on the oxygen site, Cl_O and F_O, are predicted to be shallow donors, with (+/0) transition levels above the conduction-band minimum and low formation energies under O-poor conditions. Halogen-native-defect complexes can be thermodynamically bound and provide possible compensation or passivation channels, but their impact on the carrier concentration depends on their equilibrium abundance and charge-state distribution. Self-consistent charge-neutrality calculations show that both Cl and F substitutional donors can sustain *n*-type conditions under the freeze-in treatment considered here, with the charge balance dominated by ionized substitutional donors and free electrons. Large vacancy-mediated migration barriers further indicate that substitutional halogen donors are kinetically stable after incorporation. These results provide a microscopic description of the thermodynamic, electronic, and kinetic factors governing Cl and F doping in ZnO.

DOI: 10.1103/7ts3-ktb3

I. INTRODUCTION

Zinc oxide (ZnO) is a prototypical wide-band-gap semiconductor ($E_g \approx 3.3$ eV) with high optical transparency, a large exciton binding energy (60 meV), and robust thermal and chemical stability [1]. These properties make ZnO a highly attractive material for a wide range of optoelectronic applications, including ultraviolet photodetectors, transparent electronics, piezoelectric devices, and light-emitting diodes [2,3]. Historically, the ubiquitous unintentional *n*-type conductivity observed in as-grown ZnO was attributed to native donor defects, namely, oxygen vacancies (V_O) and zinc interstitials (Zn_i) [4,5]. However, first-principles calculations show that those native defects alone cannot provide the high electron concentrations frequently observed experimentally. Specifically, V_O is a deep donor that cannot contribute to room-temperature conductivity, and Zn_i is thermodynamically unstable and highly mobile [6]. High electron concentrations, such as those exceeding 4×10^{19} cm^{-3} reported by Look *et al.* in nominally undoped samples grown under Zn-rich conditions, are now believed to originate from unintentional background impurities and stabilized defect complexes [7]. Alongside this, ubiquitous background hydrogen is well-known to act exclusively as a shallow donor, but its behavior is highly site-dependent. Interstitial hydrogen (H_i) is highly mobile and prone to out-diffusion, leading to thermal instability under operating conditions. While substitutional hydrogen (H_O) forms a stable multicenter bond within an oxygen vacancy, its incorporation is fundamentally limited by the thermodynamic availability of these native vacancies [8–12]. The inherent unreliability and physical constraints of these unintentional doping mechanisms motivate the continued search for alternative, engineered extrinsic dopants capable of generating highly stable shallow donor states [13–16].

In contrast to its robust *n*-type behavior, achieving stable and reproducible *p*-type conductivity in ZnO remains a formidable challenge, characteristic of the doping asymmetry common in wide-band-gap oxides [17]. Numerous attempts using group-I (Li, Na) [18–22] and group-V (N, P, As) [20,23–28] dopants have generally failed to yield practical hole concentrations. These efforts are fundamentally hindered by the formation of deep acceptor levels, strong spontaneous compensation by native donor defects, and inherently low dopant solubility. These severe thermodynamic and kinetic limitations make reliable *p*-type ZnO exceedingly difficult to realize under equilibrium conditions [17,29,30]. Research efforts have increasingly focused on maximizing the material's inherent unipolarity. Optimizing and stabilizing highly degenerate *n*-type conductivity remains the primary objective for advancing ZnO-based transparent electronic and optoelectronic applications [2,3].

To achieve this, halogen elements, particularly Cl and F, have emerged as highly promising extrinsic donor candidates. There are numerous experimental reports demonstrating enhanced *n*-type conductivity of ZnO using these two elements [13–15,31–38]. Despite these encouraging results, the microscopic behavior of halogen dopants in ZnO is still not fully understood. In particular, photoluminescence studies on halogen-doped or implanted ZnO have reported

*Contact author: pakpoom.r@ku.ac.th

alternative bound-exciton features after high-temperature annealing, which were tentatively attributed to halogen-related defect complexes [39]. However, bound-exciton signatures measured at cryogenic temperatures do not uniquely identify the thermodynamic charge transition levels of the underlying defects, and the relationship between these optical features and electrically active donors remains unclear.

Moreover, many previous theoretical studies have focused primarily on isolated halogen-related defects, such as substitutional and interstitial configurations, while largely neglecting the possible formation of defect complexes under realistic growth or processing conditions [40–42]. In addition to isolated point defects, halogen impurities may associate with native defects, particularly zinc vacancies (V_{Zn}), to form complexes that can influence compensation and the resulting carrier concentration [3]. A systematic understanding of the thermodynamic stability and kinetic relevance of such complexes remains incomplete.

While numerous theoretical studies have examined point defects and dopants in ZnO, many of them focused primarily on defect energetics evaluated at fixed Fermi levels or did not explicitly distinguish between growth and operating conditions. In practice, defect populations are established at elevated temperatures during synthesis and subsequently quenched during cooling, while charge states and free carriers continue to equilibrate [43,44]. Furthermore, kinetically stable defect configurations may persist even when they are not thermodynamically favored at low temperature. A consistent treatment that combines defect thermodynamics, kinetics, and charge neutrality is therefore essential for identifying which defects ultimately control carrier concentrations in wide-band-gap semiconductors [45].

To clarify the microscopic mechanisms governing halogen doping in ZnO, we investigate Cl- and F-related defects using hybrid density functional theory. We examine how defect thermodynamics, defect association, and kinetic stability jointly determine the effectiveness of halogen donors. Both isolated halogen defects and representative halogen-native defect complexes are analyzed under oxygen-rich and oxygen-poor conditions. Formation energies, charge-transition levels, and equilibrium carrier concentrations are evaluated within a self-consistent charge-neutrality framework. In addition, vacancy-mediated migration barriers are calculated to assess the kinetic stability of substitutional halogen donors. Together, these results provide a microscopic basis for understanding the shallow-donor behavior of Cl and F in ZnO, the intrinsic compensation channels considered in this work, and the kinetic stability of substitutional halogen donors after incorporation.

II. COMPUTATIONAL DETAILS

All calculations were performed within the generalized Kohn-Sham framework, using the Heyd, Scuseria, and Ernzerhof (HSE) hybrid functional as implemented in the Vienna *ab initio* Simulation Package [46,47]. In the HSE functional, the exchange interaction is separated into short-range and long-range components using a screening parameter $\omega = 0.2\,\text{Å}^{-1}$ [48]. A fraction of nonlocal Hartree-Fock exchange is mixed with the Perdew-Burke-Ernzerhof (PBE) generalized gradient approximation for the short-range exchange, and the long-range exchange and correlation terms are described by the PBE functional. The Hartree-Fock mixing parameter was set to 0.36, yielding a band gap of 3.29 eV for wurtzite ZnO, in good agreement with the experimental value [2].

TABLE I. Calculated structural parameters, formation enthalpy ΔH^f, and band gap E_g of bulk ZnO by the PBE and HSE functionals. Available experimental values are also listed.

Properties	Experiment	PBE	HSE
a (Å)	3.25[a]	3.29	3.25
c/a	1.60[a]	1.61	1.60
ΔH^f (eV/f.u.)	−3.63[b]	−2.87	−3.22
E_g (eV)	3.3[c]	0.72	3.29

[a]References [50,53].
[b]Reference [54].
[c]References [2,55].

Projector augmented-wave potentials were employed to describe the electron–ion interaction [49]. The Zn 3d electrons were explicitly treated as valence states. Structural relaxations were performed until the residual forces on all atoms were less than $0.02\,\text{eV}\,\text{Å}^{-1}$. The optimized lattice parameters of bulk wurtzite ZnO, $a = 3.25\,\text{Å}$ and $c/a = 1.61$, are in good agreement with experimental values [50]. Defect calculations were carried out using a 96-atom supercell. The defect supercells used in the HSE calculations were constructed from the HSE-relaxed primitive-cell lattice parameters. The PBE lattice parameters reported in Table I are provided only for comparison and were not used for the HSE defect formation-energy calculations. A plane-wave energy cutoff of 400 eV and a Monkhorst–Pack $2 \times 2 \times 2$ k-point mesh were used. All calculations were performed spin polarized. To assess finite-size effects, the formation energies of the dominant substitutional donors Cl_O and F_O were also calculated using a larger 192-atom supercell. The resulting formation energies and transition levels differ by less than 0.05 eV compared to the 96-atom results (see Table S1 in the Supplemental Material [51]), indicating that finite-size effects are small.

Initial defect structures were generated by placing impurities or vacancies on the corresponding lattice or interstitial sites, followed by full ionic relaxation. To avoid imposing artificial high-symmetry configurations, symmetry-broken initial structures were also tested for point defects by applying small local displacements to neighboring atoms. For defect complexes, symmetry-inequivalent nearest-neighbor arrangements of the constituent defects were examined. All candidate structures were fully relaxed, and the formation and binding energies reported below correspond to the lowest-energy relaxed structures obtained from these initial configurations.

To determine the likelihood of halogen impurities, i.e., substitutions, interstitials, and complexes, we compute the formation energy as a function of the Fermi level, which is also dependent on the chemical potential of corresponding elements. The defect thermodynamic transition level was calculated using the standard procedure outlined in Ref. [45]. For example, the formation energy of a substitutional halogen X_O

($X = \mathrm{Cl}, \mathrm{F}$) in charge state q is given by

$$E^f\left(X_\mathrm{O}^q\right) = E_\mathrm{tot}\left(X_\mathrm{O}^q\right) - E_\mathrm{tot}(\mathrm{ZnO}) - \mu_X + \mu_O + q(\varepsilon_F + \varepsilon_\mathrm{VBM}) + \Delta^q, \quad (1)$$

where $E_\mathrm{tot}(X_\mathrm{O}^q)$ is the total energy of the supercell containing the halogen X in charge state q, and $E_\mathrm{tot}(\mathrm{ZnO})$ is the total energy of the defect-free supercell. The chemical potentials of Zn and O were constrained by the thermodynamic equilibrium condition for ZnO formation with the formation enthalpy $\Delta H_f(\mathrm{ZnO}) = \tilde{\mu}_\mathrm{Zn} + \tilde{\mu}_\mathrm{O}$, where $\tilde{\mu}_\mathrm{Zn} = \mu_\mathrm{Zn} - E_\mathrm{tot}[\mathrm{Zn_{bulk}}]$ and $\tilde{\mu}_\mathrm{O} = \mu_\mathrm{O} - E_\mathrm{tot}[\mathrm{O_2}]/2$ are the chemical potentials referenced to the total energy per atom of bulk Zn and the O_2 molecule, respectively. The O-rich and O-poor conditions correspond to $\tilde{\mu}_\mathrm{O} = 0$ and $\tilde{\mu}_\mathrm{O} = \Delta H_f(\mathrm{ZnO})$, respectively. For halogen doping, the chemical potentials of Cl and F were referenced to $ZnCl_2$ and ZnF_2, respectively, which represent realistic halogen reservoirs under typical ZnO growth conditions and impose more restrictive upper bounds on the halogen chemical potentials than elemental Cl_2 or F_2. The halogen chemical potentials were therefore defined as $\tilde{\mu}_\mathrm{Cl} = \frac{(\Delta H_f(\mathrm{ZnCl_2}) - \tilde{\mu}_\mathrm{Zn})}{2}$ and $\tilde{\mu}_\mathrm{F} = \frac{(\Delta H_f(\mathrm{ZnF_2}) - \tilde{\mu}_\mathrm{Zn})}{2}$. The resulting chemical potential limits corresponding to O-rich and O-poor growth conditions are summarized in Table S2 in the Supplemental Material [51]. Since defects can occur in charge states other than neutral, the formation energy also depends on the Fermi level (ε_F), which represents the energy of the electron reservoir. Following convention, we referenced ε_F to the valence-band maximum (ε_VBM). Charged-defect finite-size corrections were applied using the FNV scheme with the experimental static dielectric constant of ZnO (8.91) [52]. This value includes both electronic and ionic screening. We note that the dielectric constant was not computed self-consistently at the HSE level; however, using the experimental static dielectric constant is a reasonable approximation for the present charged-defect corrections and is not expected to alter the relative defect-energy trends discussed below. The charge states considered for each native defect, halogen impurity, and defect complex are listed in Table S3 of the Supplemental Material, together with representative formation energies under O-rich and O-poor limits and the finite-size correction term (Δ^q) applied to each charged-defect calculation [51].

III. RESULTS AND DISCUSSION

A. Bulk ZnO and local structure of substitutional halogens

To validate the computational approach used for defect calculations, we first examine the structural and electronic properties of bulk wurtzite ZnO. Table I summarizes the calculated lattice parameters, formation enthalpy, and band gap obtained using both the PBE and HSE functionals, together with available experimental data. While PBE significantly underestimates the band gap, HSE with a Hartree-Fock mixing parameter of 36% yields a band gap of 3.29 eV, in close agreement with the experimental value of ~3.3 eV [2,55]. The HSE functional also provides improved agreement for the lattice parameters and formation enthalpy compared to PBE. Building upon this validated description of the bulk lattice, we next examine the local atomic structural relaxations associated with the halogen substitutions.

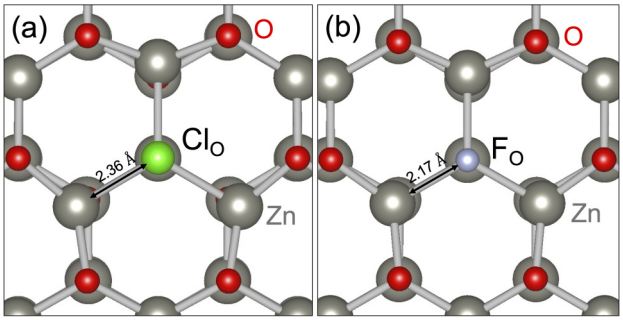

FIG. 1. Relaxed atomic structures of substitutional halogen impurities in wurtzite ZnO: (a) Cl substituting for O (Cl_O) and (b) F substituting for O (F_O) in the + charge state. The structures are viewed along the [0001] direction of the ZnO crystal. Representative basal Zn-Cl and Zn-F bond lengths are indicated.

Figure 1 illustrates the relaxed local atomic geometries of the Cl_O and F_O defects in the + charge state. In both cases, the tetrahedral coordination of the wurtzite lattice is preserved without significant structural reconstruction. Nevertheless, the two halogen substitutions induce clearly different local relaxations. For Cl_O, the Zn-Cl bond approximately oriented along the c axis is 2.42 Å, while the three basal Zn-Cl bonds are 2.361, 2.361, and 2.379 Å. For F_O, the corresponding Zn-F bond lengths are 2.212 Å and 2.166, 2.169, and 2.174 Å, respectively. Compared with the Zn-O bond length of approximately 1.98 Å in bulk ZnO, both substitutional halogens induce outward relaxation of the neighboring Zn atoms. The relaxation is anisotropic, with the apical bond longer than the basal bonds in both cases, while the small splitting among the three basal bonds indicates only a minor deviation from local threefold symmetry. The substantially larger overall bond expansion around Cl_O than F_O is consistent with the greater size mismatch introduced by Cl and suggests a larger local strain contribution to its defect energetics and association behavior discussed below.

B. Chlorine impurities and defect complexes

To elucidate the defect physics of chlorine-doped ZnO, we calculated the formation energies of isolated Cl-related defects and their complexes under O-rich and O-poor growth conditions. Figure 2 presents the formation energies as a function of the Fermi level for substitutional chlorine on the oxygen site (Cl_O), interstitial chlorine (Cl_i), substitutional chlorine on the zinc site (Cl_{Zn}), and representative defect complexes, including $Cl_O - V_{Zn}$, $2Cl_O - V_{Zn}$, $Cl_O - O_i$, and $Cl_O - Cl_i$. Intrinsic defects, such as oxygen vacancy (V_O) and zinc vacancy (V_{Zn}), are also included for comparison to assess defect competition and compensation.

Among the defects considered, Cl_O exhibits the lowest formation energy across a wide range of Fermi levels under both O-rich and O-poor conditions, with particularly favorable energetics under O-poor growth conditions. This indicates that Cl_O is the most probable chlorine-related defect formed under typical n-type growth environments. The (+/0) charge transition level of Cl_O lies above the conduction-band minimum (CBM), confirming its shallow donor character. Consequently,

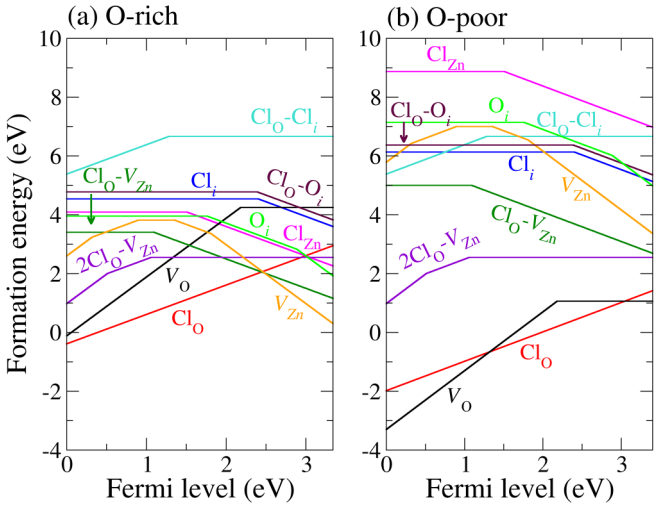

FIG. 2. Formation energies of chlorine-related defects and complexes in ZnO as a function of the Fermi level under (a) O-rich and (b) O-poor growth conditions.

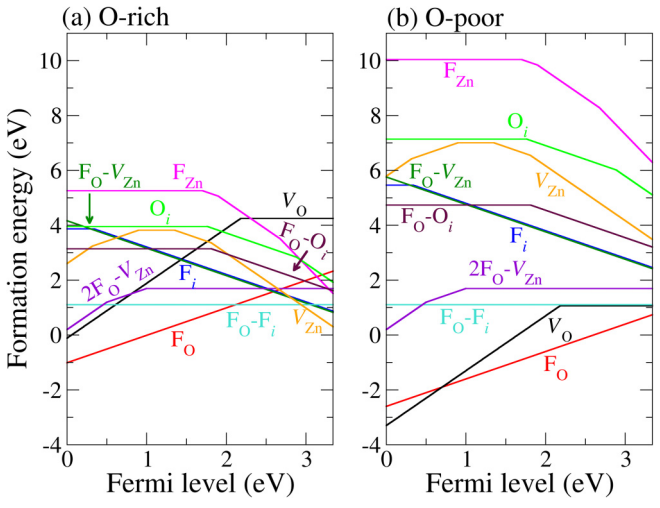

FIG. 3. Formation energies of fluorine-related defects and complexes in ZnO as a function of the Fermi level under (a) O-rich and (b) O-poor growth conditions.

Cl_O is expected to serve as an efficient, thermally active electron donor in ZnO.

In contrast, other Cl-related point defects, such as Cl_{Zn} and Cl_i, exhibit significantly higher formation energies, making them thermodynamically unfavorable under equilibrium conditions.

Furthermore, they introduce deep charge transition levels within the band gap. Specifically, Cl_{Zn} displays a (0/−) transition at 1.51 eV above the valence-band maximum (VBM), while Cl_i exhibits a (0/−) transition at 2.40 eV above the VBM, close to the CBM. These deep levels indicate that these defects, even if they are formed, do not contribute free carriers at room temperature. Zinc vacancies are well-known compensating acceptors in *n*-type ZnO. Previous hybrid-functional studies have shown that V_{Zn} is a deep, polaronic acceptor that can stabilize multiple charge states across the band gap. To allow a direct comparison with these studies, we recalculated V_{Zn} including the 2+, +, neutral, −, and 2− charge states. The calculated transition levels are (2+/+) = 0.319 eV, (+/0) = 0.897 eV, (0/–) = 1.354 eV, and (–/2–) = 1.810 eV above the VBM. These values are in good agreement with the hybrid-functional results of Lyons *et al.* [56], who reported the corresponding levels at 0.23, 0.81, 1.39, and 1.84 eV above the VBM, and are also consistent with the similar transition levels reported by Frodason *et al.* [57]. This agreement confirms that the present calculations reproduce the established deep-acceptor behavior of V_{Zn}, with negatively charged states becoming stable in the upper part of the band gap. Thus, under *n*-type conditions, V_{Zn} acts as an efficient compensating acceptor for substitutional halogen donors.

To examine possible complex formation, we investigated several Cl-related complexes, including $Cl_O - V_{Zn}$, $2Cl_O - V_{Zn}$, $Cl_O - Cl_i$, $Cl_O - Zn_i$, and $Cl_O - O_i$. The $Cl_O - Zn_i$ complex is not appreciably bound, with negative or nearly zero binding energies, and is therefore not shown in the formation-energy diagram. In contrast, the $Cl_O - V_{Zn}$ complex is energetically favorable, reflecting the Coulombic attraction between donorlike Cl_O and acceptorlike V_{Zn}. This complex exhibits a (0/−) transition level at 1.09 eV above the VBM, similar to isolated V_{Zn}, indicating that it remains a deep acceptor. The $2Cl_O - V_{Zn}$ complex exhibits (2+/+) and (+/0) transition levels at 0.51 and 1.06 eV above the VBM, respectively, confirming that it also introduces deep electronic levels and does not contribute to shallow donor behavior. The $Cl_O - Cl_i$ complex is a deep donor, with a (+/0) transition level at 1.28 eV above the VBM. However, its high formation energy under both O-rich and O-poor conditions indicates low thermodynamic stability, and its deep transition level suggests limited relevance for enhancing *n*-type conductivity. The $Cl_O - O_i$ complex is a deep acceptor, with a (0/–) transition level at 2.39 eV above the VBM. However, its formation energy remains higher than that of isolated Cl_O under both O-rich and O-poor conditions, indicating that this complex is unlikely to serve as an important compensation channel for the dominant substitutional donor.

Finally, the oxygen vacancy V_O exhibits a (2+/0) transition level at 2.18 eV above the VBM, confirming its nature as a deep donor, consistent with previous hybrid-DFT calculations [56,58]. Although its formation energy decreases under O-poor conditions, it remains higher than that of Cl_O, and its deep donor level renders it ineffective as a source of free electrons at room temperature. Accordingly, Cl_O is the only chlorine-related defect that is both energetically favorable and electrically active. In contrast, other Cl-related point defects and complexes are thermodynamically less stable and introduce deep levels that do not affect the equilibrium carrier concentration.

C. Fluorine impurities and defect complexes

To investigate the defect physics of fluorine-doped ZnO, we calculated the formation energies of isolated F-related defects and their complexes under O-poor and O-rich growth conditions. Figure 3 shows the formation energies as a function of the Fermi level for substitutional fluorine on the oxygen site (F_O), interstitial fluorine (F_i), substitutional

fluorine on the zinc site (F_{Zn}), and representative defect complexes, including $F_O - V_{Zn}$, $2F_O - V_{Zn}$, $F_O - O_i$, and $F_O - F_i$. Intrinsic point defects, V_O and V_{Zn} are also included for comparison to assess defect competition and compensation effects. Among all fluorine-related defects, F_O exhibits the lowest formation energy under both O-rich and O-poor conditions, with particularly favorable energetics under O-poor growth conditions. This indicates that F_O is the most probable fluorine-related defect to form under typical *n*-type growth environments. Similar to Cl_O, F_O remains stable in the 1+ charge state across the entire Fermi-level range and does not exhibit any charge transition level within the band gap. This confirms its shallow donor character and identifies F_O as a source of free electrons in ZnO.

Other fluorine-related point defects are significantly less favorable. Substitutional fluorine on the zinc site, F_{Zn}, exhibits high formation energies and multiple acceptorlike charge transition levels, including (0/−), (−/2−), and (2−/3−) transitions located deep within the band gap. These characteristics indicate that F_{Zn} behaves as a deep acceptor and does not contribute to *n*-type conductivity. Interstitial fluorine, F_i, also has a relatively high formation energy and exhibits a (0/−) transition at 0.34 eV above the valence-band maximum. Although this level is closer to the band edge than those of F_{Zn}, it remains too deep to contribute significantly to hole conduction at room temperature. It thus plays a negligible role in carrier compensation.

The role of zinc vacancies is consistent with the trends observed in Cl-doped ZnO. As discussed above, V_{Zn} is a deep acceptor with multiple charge-transition levels across the band gap. In the relevant *n*-type Fermi-level range, the negatively charged states are thermodynamically stable and can in principle compensate donor defects such as F_O. However, the revised charge-neutrality calculations show that the equilibrium concentration of V_{Zn} remains low over the chemical-potential range considered and does not dominate the charge balance. Under O-poor conditions, its formation energy increases further, suppressing its concentration and favoring donor activation.

We further examine fluorine-related defect complexes, including $F_O - V_{Zn}$, $2F_O - V_{Zn}$, $F_O - F_i$, $F_O - Zn_i$, and $F_O - O_i$. The $F_O - Zn_i$ complex is not appreciably bound, with negative or nearly zero binding energies, and is therefore not shown in the formation-energy diagram. In contrast, the $F_O - V_{Zn}$ complex is energetically favorable, reflecting the Coulombic attraction between donorlike F_O and acceptor-like V_{Zn}. This complex is stable in the negative charge state over much of the relevant Fermi-level range and can act as a compensating center for the F_O donor. The $2F_O - V_{Zn}$ complex exhibits (2+/+) and (+/0) transition levels at 0.50 and 1.00 eV above the VBM, respectively, indicating that it acts as a deep donor.

The $F_O - F_i$ complex was also considered. It has a moderate formation energy and remains electronically inactive over the Fermi-level range of interest, as indicated by the absence of charge-transition levels. Accordingly, it is not expected to play a significant role in carrier compensation or activation. The $F_O - O_i$ complex behaves as a deep acceptor, with a (0/−) transition level at approximately 1.81 eV above the VBM. Under O-poor conditions, its formation energy remains higher than that of F_O. Under O-rich conditions and for Fermi levels near the CBM, $F_O - O_i$ can become lower in formation energy than isolated F_O; however, the charge-neutrality analysis shows that this complex does not appreciably affect the calculated Fermi level or carrier concentration. Finally, the intrinsic oxygen vacancy V_O exhibits a deep (2+/0) transition level at 2.18 eV above the VBM. Although its formation energy is lower under O-poor conditions, it remains less favorable than F_O and is not the dominant source of free electrons in the present calculations. These results indicate that substitutional F_O is the dominant electrically active fluorine-related donor, while the other fluorine-related defects and complexes mainly provide possible compensation or passivation channels whose actual importance is assessed through the charge-neutrality analysis below.

The shallow-donor character of Cl_O and F_O obtained in the present calculations contrasts with earlier theoretical results for halogen impurities in ZnO. Previous LDA-based calculations reported donor levels within the band gap for substitutional halogens. In particular, F_O was predicted to be a deep donor with an activation energy of 0.76 eV below the CBM, leading to the conclusion that it could not directly account for the enhanced electron concentration in F-doped ZnO [40]. Similarly, earlier calculations for Cl-doped ZnO concluded that neither Cl_O nor Cl_i directly contributes to increased carrier concentrations [41]. In contrast, the present hybrid-functional calculations place the (+/0) transition levels of Cl_O and F_O at 0.52 and 0.42 eV above the calculated CBM, respectively, identifying both substitutional halogens as shallow donors. These results indicate that the predicted donor character is sensitive to the description of the ZnO electronic structure and band-edge positions. The convergence of the calculated transition levels with respect to supercell size is summarized in Table S1 of the Supplemental Material [51].

D. Binding energies and thermodynamic stability of halogen-related defect complexes

To further assess the thermodynamic stability of halogen-related defect complexes in ZnO, we evaluated their binding energies, which quantify the energetic preference for isolated point defects to associate and form complexes. This analysis is particularly relevant for understanding donor-acceptor interactions and their possible impact on defect populations under equilibrium growth conditions. The binding energy (E_b) of a defect complex is defined as the energy gained upon association of its isolated constituents. For example, for the $Cl_O - V_{Zn}$ complex in the negative charge state, the binding energy is given by

$$E_b(Cl_O - V_{Zn})^- = E^f\left(Cl_O^+\right) + E^f\left(V_{Zn}^{2-}\right) - E^f(Cl_O - V_{Zn})^-, \tag{2}$$

where $E^f(Cl_O - V_{Zn})^-$ is the formation energy of the $Cl_O - V_{Zn}$ complex in the – charge state, $E^f(Cl_O^+)$ is the formation energy of Cl_O in the + charge state, and $E^f(V_{Zn}^{2-})$ is the formation energy of V_{Zn} in the 2– charge state. A positive binding energy indicates that complex formation is thermodynamically favorable.

TABLE II. Calculated binding energies E_b (in eV) of representative halogen-related defect complexes in ZnO for charge states q. Positive binding energies indicate thermodynamically stable (bound) complexes, while negative values indicate unbound configurations. Here $X = \mathrm{Cl}$ or F.

Complex	q	E_b ($X = \mathrm{Cl}$)	E_b ($X = \mathrm{F}$)
$X_\mathrm{O} - V_\mathrm{Zn}$	−	2.09	1.80
	0	1.37	
$2X_\mathrm{O} - V_\mathrm{Zn}$	0	3.65	3.26
	+	2.09	2.45
	2+	2.40	1.94
$X_\mathrm{O} - X_i$	0	−0.11	2.09
	+	−1.13	
$X_\mathrm{O} - \mathrm{O}_i$	−	1.05	2.64
	0	0.55	1.56

The calculated binding energies of representative chlorine- and fluorine-related complexes are summarized in Table II. For chlorine-related defects, the $\mathrm{Cl_O} - V_\mathrm{Zn}$ complex exhibits positive binding energies in both the neutral and − charge states, indicating that donor-acceptor association is energetically favorable due to Coulombic attraction between the positively charged $\mathrm{Cl_O}$ donor and the negatively charged V_Zn. The $2\mathrm{Cl_O} - V_\mathrm{Zn}$ complex shows even larger positive binding energies across all examined charge states, reflecting enhanced stabilization when an additional donor is introduced. In contrast, the $\mathrm{Cl_O} - \mathrm{Cl}_i$ complex has negative binding energy, indicating that it is thermodynamically unfavorable and unlikely to form at significant concentrations.

A similar trend is observed for fluorine-related complexes. The $\mathrm{F_O} - V_\mathrm{Zn}$ complex is thermodynamically stable only in the – charge state, as indicated by a positive binding energy, whereas the neutral configuration has a very small binding energy and is therefore weakly bound or unstable. The $2\mathrm{F_O} - V_\mathrm{Zn}$ complex shows positive binding energies across all charge states considered, indicating a strong donor-acceptor interaction, analogous to the chlorine case. The $\mathrm{F_O} - \mathrm{F}_i$ complex shows a positive binding energy in the neutral charge state; however, no binding energy is reported for the + charge state because it is not thermodynamically stable within the band gap.

Several donor-acceptor complexes involving $\mathrm{Cl_O}$, $\mathrm{F_O}$, O_i, and V_Zn are energetically bound, indicating that their formation can contribute to donor compensation during growth. It is important to distinguish the charge-transition levels of these complexes from their effect on the net donor population. The $\mathrm{Cl_O} - V_\mathrm{Zn}$, $\mathrm{F_O} - V_\mathrm{Zn}$, $\mathrm{Cl_O} - \mathrm{O}_i$, and $\mathrm{F_O} - \mathrm{O}_i$ complexes act as acceptorlike compensating centers, whereas the $2\mathrm{Cl_O} - V_\mathrm{Zn}$ and $2\mathrm{F_O} - V_\mathrm{Zn}$ complexes retain donorlike transition levels. In either case, complex formation can reduce the concentration of electrically active isolated donors through association of $\mathrm{Cl_O^+}$ or $\mathrm{F_O^+}$ with zinc vacancies. For example, in the binding-energy analysis, the negatively charged $\mathrm{Cl_O} - V_\mathrm{Zn}$ complex is referenced to isolated $\mathrm{Cl_O^+}$ with V_Zn^{2-}, conserving the total charge of the complex. However, binding energies alone do not determine the net carrier concentration under a given growth condition. The actual importance of these complexes depends on their equilibrium abundance and charge-state distribution, which are evaluated below using the self-consistent charge-neutrality analysis.

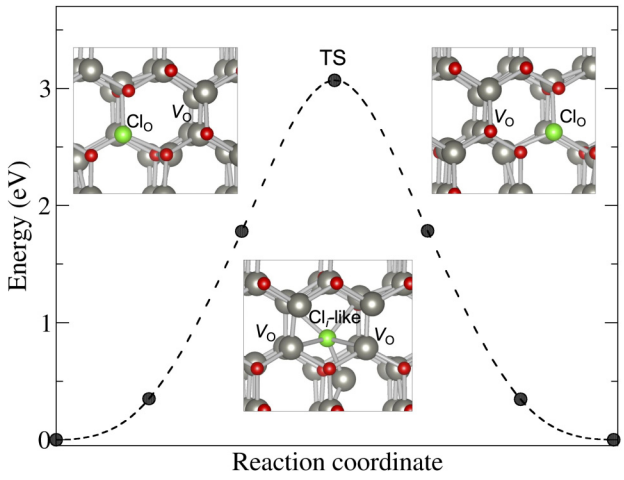

FIG. 4. Minimum-energy path for oxygen-vacancy-mediated migration of $\mathrm{Cl_O}$ in ZnO in the + charge state, obtained using the CI-NEB method. Insets show atomic configurations of the initial state, saddle point, and final state. The saddle-point geometry corresponds to a transient interstitial-like configuration of Cl between two neighboring oxygen vacancies, characteristic of a vacancy-mediated exchange mechanism. The highest-energy image corresponds to the transition state (TS).

E. Kinetic stability of substitutional halogen donors

To assess the kinetic stability of substitutional halogen donors in ZnO, we investigated vacancy-mediated migration pathways for $\mathrm{Cl_O}$ and $\mathrm{F_O}$ using the climbing-image nudged elastic band (CI-NEB) method [59]. Because CI-NEB calculations with hybrid functionals are computationally expensive, the migration pathways were first optimized with the GGA-PBE functional, and the total energies of the resulting images were then evaluated with the HSE hybrid functional. The reported barriers should therefore be regarded as HSE-corrected barriers along the PBE minimum-energy path rather than fully HSE-optimized NEB barriers. The PBE CI-NEB barriers are 2.6 eV for $\mathrm{Cl_O}$ and 2.3 eV for $\mathrm{F_O}$, while HSE single-point energies evaluated on the same images increase these values to approximately 3.1 and 2.6 eV, respectively. Although this approximation may introduce some quantitative uncertainty, both sets of barriers are large, supporting the conclusion that vacancy-mediated migration of substitutional halogen donors is strongly suppressed at low temperature. Figure 4 shows the minimum-energy path for V_O-mediated migration of $\mathrm{Cl_O}$ in the + charge state, which is the dominant charge state under n-type conditions. The calculated migration barrier is approximately 3.1 eV, indicating that $\mathrm{Cl_O}$ is kinetically stable against diffusion even in the presence of an adjacent oxygen vacancy. Inspection of the atomic configurations along the migration pathway shows that the saddle-point geometry corresponds to a transient interstitial-like configuration, in which the Cl atom occupies a position between two neighboring oxygen vacancies, resembling a $V_\mathrm{O} - \mathrm{Cl}_i$-like-$V_\mathrm{O}$ arrangement. This configuration is not a stable defect but represents the transition state of the vacancy-mediated

exchange process, also reported in other semiconductors such as CdTe [43]. It is important to note that the effective activation energy for vacancy-mediated halogen diffusion depends on whether the assisting oxygen vacancy is generated during the diffusion process or is already present in the sample. If the oxygen vacancy must be thermally generated, the activation energy may be approximated as $E_a = E_m + E^f(V_O)$, where E_m is the vacancy-mediated migration barrier and $E^f(V_O)$ is the formation energy of the oxygen vacancy under the relevant chemical-potential and Fermi-level conditions. Using $E_m \approx 3.1$ eV for Cl_O and $E^f(V_O) \approx 1$ eV near the CBM under the O-poor condition gives an effective activation energy of approximately 4.1 eV. If oxygen vacancies are already present, for example, as frozen-in defects from growth, the relevant hopping barrier is instead E_m, while the overall diffusion rate is controlled by the concentration of available oxygen vacancies. Even in this limit, the calculated hopping barrier of approximately 3.1 eV remains large, indicating that vacancy-mediated migration of Cl_O is strongly suppressed at low-temperature or device-operation conditions.

A similar vacancy-mediated pathway for F_O gives a migration barrier of approximately 2.6 eV. This barrier is lower than that for Cl_O, but it is still sufficiently large to suppress long-range migration under low-temperature or device-operation conditions, especially when the concentration of available oxygen vacancies is limited. If oxygen vacancies must be generated thermally, the effective activation energy further includes $E^f(V_O)$, leading to an even larger activation energy. These results indicate that substitutional Cl_O and F_O are kinetically stable after incorporation, although the quantitative activation energy for vacancy-mediated diffusion depends on the oxygen-vacancy concentration, growth conditions, and Fermi-level position.

We also considered a possible dissociation pathway in which substitutional chlorine leaves the oxygen site to form an interstitial chlorine and an oxygen vacancy, $Cl_O \rightarrow Cl_i + V_O$. Starting from configurations in which the Cl atom was displaced from the oxygen site toward a nearby interstitial position, structural relaxation returned the system to the substitutional Cl_O configuration. This indicates that the separated $Cl_i + V_O$ configuration is not a stable local minimum for the configurations examined. Therefore, diffusion through dissociation into a mobile Cl_i is unlikely to compete with the vacancy-mediated exchange pathway considered above.

F. Charge neutrality and carrier concentrations

Given the large vacancy-mediated migration barriers discussed above, defect configurations formed during growth are expected to be preserved upon cooling. We therefore evaluate equilibrium defect concentrations and the Fermi-level position at a representative growth temperature of 800 K, which lies within the typical temperature range used for ZnO synthesis and processing [2,3]. The equilibrium Fermi level at a given temperature and oxygen chemical potential is determined by enforcing the charge neutrality condition,

$$n - p + \sum_i \sum_q q\mathrm{N}_i^q = 0, \tag{3}$$

where n and p are the free electron and hole concentrations, respectively, and N_i^q denotes the concentration of defect i in charge state q. The carrier concentrations are evaluated by integrating the electronic density of states, $D(E)$, obtained from HSE calculations using Fermi-Dirac statistics:

$$n = \int_{\varepsilon_{CBM}}^{\infty} D(\varepsilon)\left(\frac{1}{\exp[(\varepsilon - \varepsilon_F)/k_BT] + 1}\right)d\varepsilon \quad \text{and}$$
$$p = \int_{-\infty}^{\varepsilon_{VBM}} D(\varepsilon)\left(1 - \frac{1}{\exp[(\varepsilon - \varepsilon_F)/k_BT] + 1}\right)d\varepsilon. \tag{4}$$

Defect concentrations are computed from their formation energies, including all thermodynamically stable charge states, where ε_{CBM} and ε_{VBM} are the energy of the conduction band minimum and valence band maximum, respectively. ε_F is the Fermi level, k_B is the Boltzmann constant, and T is the absolute temperature [60]. Configurational degeneracy factors were included in the defect concentration calculations. For isolated substitutional defects and vacancies, the degeneracy was determined from the number of equivalent lattice sites. For defect complexes, the degeneracy was assigned based on the number of symmetry-equivalent relative orientations of the lowest-energy relaxed complex configuration. At the growth temperature of 800 K, full thermodynamic equilibrium is assumed. For device operating conditions at 300 K, the total concentrations of atomic defects are fixed at their growth-equilibrium values, while the Fermi level, free carriers, and defect charge-state populations are allowed to re-equilibrate.

The freeze-in approximation is supported by high migration barriers of the relevant defects, which indicate that atomic diffusion is unlikely at 300 K. Previous calculations reported barriers of 1.4 eV for V_{Zn}^{2-}, 1.7 eV for V_O^{2+}, and 2.0 eV for F_i^-. Our calculated V_O^{2+} migration barrier is also ~1.7 eV, in agreement with this earlier result. In addition, the vacancy-mediated migration barriers of substitutional halogens are much larger, approximately 3.1 eV for Cl_O and 2.6 eV for F_O. These values indicate that atomic diffusion is strongly suppressed at 300 K. We therefore freeze the total concentrations of all atomic defect species at their growth-equilibrium values and allow only the Fermi level, free carriers, and defect charge-state populations to re-equilibrate at 300 K. The total concentrations of defect complexes are treated in the same way, since changes in their abundance would require migration or dissociation of the constituent atomic defects. The defect concentrations plotted in Figs. 5 and 6 correspond to charge-state-resolved concentrations, (N_i^q), for the dominant charge states. In the 300 K freeze-in calculations, the total concentration of each defect species, $(N_i^{tot} = \sum_q N_i^q)$, is fixed at its 800 K equilibrium value, while the charge-state populations are re-equilibrated at 300 K together with the Fermi level and free-carrier concentrations.

Figure 5 shows the calculated defect concentrations and Fermi-level positions as functions of the oxygen chemical potential μ_O for Cl-doped ZnO under (a) full thermodynamic equilibrium at 800 K and (b) device conditions at 300 K with selected defects frozen at their 800 K concentrations. Only V_O, V_{Zn}, Cl_O, and the $Cl_O - V_{Zn}$ complex in all stable charge states were included in the charge-neutrality calculations, as other Cl-related point defects and complexes have significantly higher formation energies and negligible equilibrium

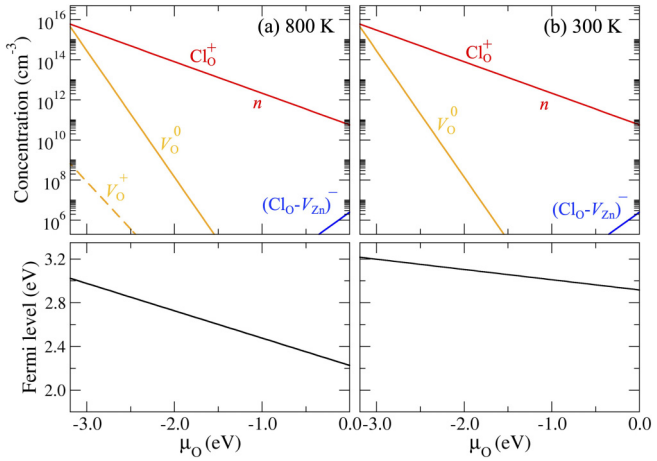

FIG. 5. Calculated defect concentrations (top panels) and Fermi level positions (bottom panels) as functions of the oxygen chemical potential μ_O for Cl-doped ZnO. (a) Full thermodynamic equilibrium at the growth temperature of 800 K. (b) Electronic equilibrium at 300 K, assuming that defect concentrations formed at 800 K are frozen in upon cooling, while free carriers are allowed to re-equilibrate. Only the dominant charge states are shown for clarity.

concentrations over the relevant range of oxygen chemical potentials.

At 800 K [Fig. 5(a)], full thermodynamic equilibrium is established among all defects and carriers. Under O-poor conditions, the substitutional donor Cl_O^+ is the dominant Cl-related species, reaching concentrations above 10^{16} cm^{-3}, and the electron concentration closely follows the ionized donor population. The Fermi level, therefore, lies near the CBM. As μ_O increases toward O-rich conditions, the formation energy of Cl_O^+ rises, while compensating acceptor defects, particularly V_{Zn}^{2-} and the complex $(Cl_O - V_{Zn})^-$, become increasingly favorable. The concentration of the complex grows steadily and eventually exceeds the free-electron concentration under O-rich conditions. This enhanced compensation drives a monotonic downward shift of the Fermi level toward midgap at high temperature.

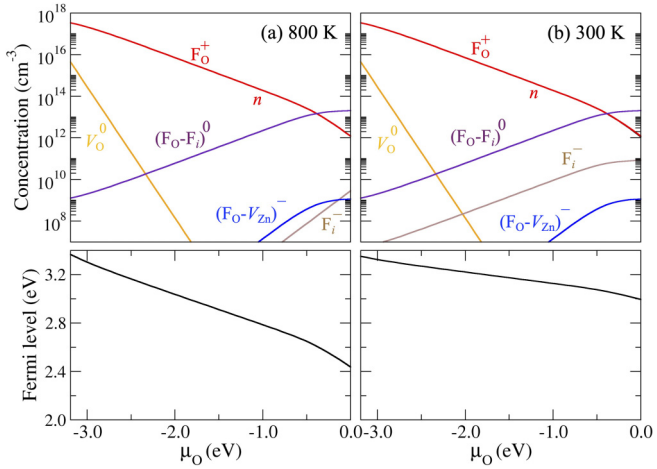

FIG. 6. Calculated defect concentrations (top panels) and Fermi level positions (bottom panels) as functions of the oxygen chemical potential μ_O for F-doped ZnO. (a) Full thermodynamic equilibrium at the growth temperature of 800 K. (b) Electronic equilibrium at 300 K, assuming that defect concentrations formed at 800 K are frozen in upon cooling, while free carriers are allowed to re-equilibrate. Only the dominant charge states are shown for clarity.

Figure 5(b) shows the electronic equilibrium at 300 K, assuming that the total concentrations of Cl_O, V_{Zn}, V_O and $Cl_O - V_{Zn}$ established at 800 K are frozen upon cooling, consistent with their large migration barriers. In contrast, the charge states and free carriers are allowed to re-equilibrate at 300 K under the charge-neutrality condition. Upon cooling, the intrinsic carrier concentration is strongly suppressed, whereas the frozen donor and acceptor populations remain fixed. Charge neutrality is therefore restored primarily through a shift of the Fermi level rather than through the redistribution of defect populations. As a result, the Fermi level at 300 K lies systematically higher than in the 800 K equilibrium case across the entire μ_O range, most prominently under O-rich conditions where compensation is strongest at high temperature. The persistence of a relatively high Fermi level and finite electron concentration at 300 K indicates that Cl_O donors remain electrically active after cooling, despite partial compensation by zinc-vacancy-related defects and complexes. These results demonstrate that Cl incorporation in ZnO produces robust n-type conductivity that remains stable across the temperature range from growth to device-operating temperatures.

Figure 6 shows the calculated defect concentrations and Fermi-level positions as functions of the oxygen chemical potential for F-doped ZnO under (a) full thermodynamic equilibrium at 800 K and (b) device conditions at 300 K with selected defects frozen at their 800 K concentrations. For these charge-neutrality calculations, V_O, V_{Zn}, F_O, the fluorine interstitial (F_i), and the two competing complexes, $F_O - V_{Zn}$ and $F_O - F_i$, were included to describe the dominant compensation and passivation mechanisms among the fluorine-related defects considered in this work.

At 800 K [Fig. 6(a)], full thermodynamic equilibrium is established. Under O-poor conditions, the behavior closely mirrors the Cl-doped system: The substitutional donor dominates, reaching high concentrations, and provides robust n-type conductivity with the Fermi level positioned near the CBM. However, as μ_O increases toward O-rich conditions, acceptor-type defects and complexes, including $(F_O - V_{Zn})^-$ and F_i^-, become more favorable and can contribute to donor compensation. Nevertheless, their concentrations remain lower than that of the ionized substitutional donor F_O^+, and the Fermi level remains in the upper part of the band gap under the conditions considered here.

At 300 K [Fig. 6(b)], the frozen donor population remains the dominant charged defect population over the chemical-potential range considered. Although fluorine-related acceptor defects and complexes become more visible toward O-rich conditions, they do not dominate the charge balance. The electron concentration therefore largely follows the concentration of F_O^+, and the Fermi level remains relatively high after cooling. The key thermodynamic, electronic, and kinetic quantities for the dominant substitutional donors are summarized in Table III.

TABLE III. Comparison of key quantities for substitutional Cl and F donors in ZnO: Dominant donor, the (+/0) transition level relative to the CBM, formation energy $E^f(X_O^+)$ at E_F = CBM and O-poor limit (eV), V_O-mediated migration barrier (E_m), estimated activation energy (E_a), and the peak calculated electron concentration n at 300 K.

Quantity	$X = Cl$	$X = F$
Dominant donor	Cl_O^+	F_O^+
(+/0) relative to CBM (eV)	+0.52	+0.42
$E^f(X_O^+)$ (eV)	1.3	0.7
E_m (eV)	∼3.1	∼2.6
E_a (eV)	∼4.1	∼3.6
Peak n at 300 K (cm^{-3})	$\sim 10^{16}$	$\sim 10^{17}$

The calculated electron concentrations should be compared with experiment with some caution. Hall measurements for the heavily doped ZnO thin films often report electron concentrations of approximately $10^{19} - 10^{20}$ cm^{-3}, depending on the growth method, dopant content, substrate, and post-growth processing [35–37,61,62]. These values are higher than the electron concentrations of order 10^{16} cm^{-3} obtained from the present equilibrium/freeze-in charge-neutrality calculations. This difference likely reflects the nonequilibrium nature of many thin-film growth methods, which can incorporate halogen dopants at concentrations above their equilibrium solubility, as well as possible contributions from unintentional hydrogen, oxygen vacancies, nonstoichiometry, grain boundaries, or extended defects. Thus, the present calculations should not be viewed as a quantitative prediction of the maximum experimentally attainable carrier density. Rather, they identify the microscopic donor character of substitutional Cl_O and F_O and the intrinsic compensation mechanisms that can limit their equilibrium doping efficiency.

These results indicate that both Cl and F can sustain n-type conditions under the freeze-in treatment considered here. In both cases, the electron concentration largely follows the concentration of ionized substitutional donors, while compensating acceptors and halogen-related complexes remain at lower concentrations. Although F-related acceptor defects and complexes are more visible than their Cl counterparts, they do not dominate the charge balance under the present thermodynamic conditions. Thus, substitutional Cl_O and F_O are both effective shallow donors within the intrinsic-defect model considered here, with compensation controlled by the equilibrium abundance of native defects and defect complexes.

IV. CONCLUSION

In summary, we have systematically examined chlorine- and fluorine-related defects in ZnO by combining defect thermodynamics, defect association, vacancy-mediated migration barriers, and self-consistent charge-neutrality analysis across growth and operating temperatures. Both Cl_O and F_O are identified as shallow donors with low formation energies under O-poor conditions and no charge-transition levels within the band gap. In contrast, halogen-related complexes and compensating native defects introduce deep levels and, although in some cases thermodynamically bound, do not control the equilibrium carrier concentration. The large vacancy-mediated migration barriers indicate strong kinetic stability of substitutional halogen donors, supporting freeze-in of growth-established defect populations. Charge-neutrality calculations incorporating growth-temperature equilibration and subsequent cooling demonstrate that n-type conductivity persists over a wide range of oxygen chemical potentials. These results provide a coherent microscopic understanding of halogen doping in ZnO and clarify how thermodynamic stability, defect association, and kinetic constraints collectively govern dopant effectiveness in wide-band-gap oxides.

ACKNOWLEDGMENTS

This work was supported by the Kasetsart Research and Development Institute (KURDI) through Fundamental Funds [FF(KU)55.69]. S.C. thanks I. Watanabe for the support and computing resource (HOKUSAI) at RIKEN. P.R. thanks J.T-Thienprasert for the fruitful discussion. We thank the NSTDA Supercomputer Center (ThaiSC) for providing computing resources for this work.

DATA AVAILABILITY

The data that support the findings of this article are not publicly available. The data are available from the authors upon reasonable request.

[1] C. Klingshirn, ZnO: From basics towards applications, phys. stat. sol. (b) **244**, 3027 (2007).

[2] Ü. Özgür, Y. I. Alivov, C. Liu, A. Teke, M. A. Reshchikov, S. Doğan, V. Avrutin, S.-J. Cho, and H. Morkoç, A comprehensive review of ZnO materials and devices, J. Appl. Phys. **98**, 041301 (2005).

[3] A. Janotti and C. G. Van de Walle, Fundamentals of zinc oxide as a semiconductor, Rep. Prog. Phys. **72**, 126501 (2009).

[4] M. D. McCluskey and S. J. Jokela, Sources of n-type conductivity in ZnO, Physica B **401–402**, 355 (2007).

[5] L. Liu, Z. Mei, A. Tang, A. Azarov, A. Kuznetsov, Q.-K. Xue, and X. Du, Oxygen vacancies: The origin of n-type conductivity in ZnO, Phys. Rev. B **93**, 235305 (2016).

[6] A. Janotti and C. G. Van de Walle, Native point defects in ZnO, Phys. Rev. B **76**, 165202 (2007).

[7] D. C. Look, G. C. Farlow, P. Reunchan, S. Limpijumnong, S. B. Zhang, and K. Nordlund, Evidence for native-defect donors in n-type ZnO, Phys. Rev. Lett. **95**, 225502 (2005).

[8] A. Janotti and C. G. Van de Walle, Hydrogen multicentre bonds, Nat. Mater. **6**, 44 (2007).

[9] G. A. Shi, M. Saboktakin, M. Stavola, and S. J. Pearton, Hidden hydrogen in as-grown ZnO, Appl. Phys. Lett. **85**, 5601 (2004).

[10] C. G. Van de Walle, Hydrogen as a cause of doping in zinc oxide, Phys. Rev. Lett. **85**, 1012 (2000).

[11] S. Limpijumnong, P. Reunchan, A. Janotti, and C. G. Van de Walle, Hydrogen doping in indium oxide: An *ab initio* study Phys. Rev. B **80**, 193202 (2009).
[12] P. Reunchan, X. Zhou, S. Limpijumnong, A. Janotti, and C. G. Van de Walle, Vacancy defects in indium oxide: An *ab initio* study, Curr. Appl Phys. **11**, S296 (2011).
[13] H. Y. Xu, Y. C. Liu, R. Mu, C. L. Shao, Y. M. Lu, D. Z. Shen, and X. W. Fan, F-doping effects on electrical and optical properties of ZnO nanocrystalline films, Appl. Phys. Lett. **86**, 123107 (2005).
[14] P. M. Ratheesh Kumar, C. Sudha Kartha, K. P. Vijayakumar, F. Singh, and D. K. Avasthi, Effect of fluorine doping on structural, electrical and optical properties of ZnO thin films, Mater. Sci. Eng. B **117**, 307 (2005).
[15] A. Jiamprasertboon, S. C. Dixon, S. Sathasivam, M. J. Powell, Y. Lu, T. Siritanon, and C. J. Carmalt, Low-cost one-step fabrication of highly conductive ZnO:Cl transparent thin films with tunable photocatalytic properties via aerosol-assisted chemical vapor deposition, ACS Appl. Electron. Mater. **1**, 1408 (2019).
[16] S. B. Orlinskii, J. Schmidt, P. G. Baranov, V. Lorrmann, I. Riedel, D. Rauh, and V. Dyakonov, Identification of shallow Al donors in Al-doped ZnO nanocrystals: EPR and ENDOR spectroscopy, Phys. Rev. B **77**, 115334 (2008).
[17] R. Yang, F. Wang, J. Lu, Y. Lu, B. Lu, S. Li, and Z. Ye, ZnO with *p*-type doping: Recent approaches and applications, ACS Appl. Electron. Mater. **5**, 4014 (2023).
[18] A. Carvalho, A. Alkauskas, A. Pasquarello, A. K. Tagantsev, and N. Setter, A hybrid density functional study of lithium in ZnO: Stability, ionization levels, and diffusion, Phys. Rev. B **80**, 195205 (2009).
[19] M. G. Wardle, J. P. Goss, and P. R. Briddon, Theory of Li in ZnO: A limitation for Li-based *n*-type doping, Phys. Rev. B **71**, 155205 (2005).
[20] C. H. Park, S. B. Zhang, and S.-H. Wei, Origin of *p*-type doping difficulty in ZnO: The impurity perspective, Phys. Rev. B **66**, 073202 (2002).
[21] S. S. Lin, J. G. Lu, Z. Z. Ye, H. P. He, X. Q. Gu, L. X. Chen, J. Y. Huang, and B. H. Zhao, *p*-type behavior in Na-doped ZnO films and ZnO homojunction light-emitting diodes, Solid State Commun. **148**, 25 (2008).
[22] N. S. Parmar and K. G. Lynn, Sodium doping in ZnO crystals, Appl. Phys. Lett. **106**, 022101 (2015).
[23] J. L. Lyons, A. Janotti, and C. G. Van de Walle, Why nitrogen cannot lead to *p*-type conductivity in ZnO, Appl. Phys. Lett. **95**, 252105 (2009).
[24] P. Li, S. Deng, G. Liu, and K. Hou, Comprehensive investigations on the feasibility of nitrogen as a *p*-type dopant in ZnO, Chem. Phys. Lett. **543**, 92 (2012).
[25] A. Boonchun, W. R. L. Lambrecht, J. T-Thienprasert, and S. Limpijumnong, Nitrogen pair-hydrogen complexes in ZnO and *p*-type doping, MRS Online Proc. Libr. **1394**, 27 (2012).
[26] W.-J. Lee, J. Kang, and K. J. Chang, Defect properties and *p*-type doping efficiency in phosphorus-doped ZnO, Phys. Rev. B **73**, 024117 (2006).
[27] F. X. Xiu, Z. Yang, L. J. Mandalapu, and J. L. Liu, Donor and acceptor competitions in phosphorus-doped ZnO, Appl. Phys. Lett. **88**, 152116 (2006).
[28] G. Braunstein, A. Muraviev, H. Saxena, N. Dhere, V. Richter, and R. Kalish, *p* type doping of zinc oxide by arsenic ion implantation, Appl. Phys. Lett. **87**, 192103 (2005).
[29] J. Robertson and S. J. Clark, Limits to doping in oxides, Phys. Rev. B **83**, 075205 (2011).
[30] J. G. Reynolds and C. L. Reynolds, Progress in ZnO acceptor doping: What is the best strategy? Adv. Condens. Matter Phys. **2014**, 457058 (2014).
[31] Y.-J. Choi and H.-H. Park, A simple approach to the fabrication of fluorine-doped zinc oxide thin films by atomic layer deposition at low temperatures and an investigation into the growth mode, J. Mater. Chem. C **2**, 98 (2014).
[32] A. B. Djurišić, A. M. C. Ng, and X. Y. Chen, ZnO nanostructures for optoelectronics: Material properties and device applications, Prog. Quantum Electron. **34**, 191 (2010).
[33] E. Chikoidze, M. Modreanu, V. Sallet, O. Gorochov, and P. Galtier, Electrical properties of chlorine-doped ZnO thin films grown by MOCVD, phys. stat. sol. (a) **205**, 1575 (2008).
[34] J. Fan, A. Shavel, R. Zamani, C. Fábrega, J. Rousset, S. Haller, F. Güell, A. Carrete, T. Andreu, J. Arbiol, *et al.*, Control of the doping concentration, morphology and optoelectronic properties of vertically aligned chlorine-doped ZnO nanowires, Acta Mater. **59**, 6790 (2011).
[35] L. Cao, L. Zhu, J. Jiang, R. Zhao, Z. Ye, and B. Zhao, Highly transparent and conducting fluorine-doped ZnO thin films prepared by pulsed laser deposition, Sol. Energy Mater. Sol. Cells **95**, 894 (2011).
[36] H. S. Yoon, K. S. Lee, T. S. Lee, B. Cheong, D. K. Choi, D. H. Kim, and W. M. Kim, Properties of fluorine doped ZnO thin films deposited by magnetron sputtering, Sol. Energy Mater. Sol. Cells **92**, 1366 (2008).
[37] T. Hurma and M. Caglar, Properties of fluorine doped ZnO thin films deposited by magnetron sputtering, Mater. Sci. Semicond. Process. **110**, 104949 (2020).
[38] A. Sanchez-Juarez, A. Tiburcio-Silver, A. Ortiz, E. P. Zironi, and J. Rickards, Electrical and optical properties of fluorine-doped ZnO thin films prepared by spray pyrolysis, Thin. Solid. Films **333**, 196 (1998).
[39] A. Azarov, A. Galeckas, V. Venkatachalapathy, Z. Mei, X. Du, E. Monakhov, and A. Kuznetsov, Acceptor complex signatures in oxygen-rich ZnO thin films implanted with chlorine ions, J. Appl. Phys. **128**, 125701 (2020).
[40] B. Liu, M. Gu, X. Liu, S. Huang, and C. Ni, First-principles study of fluorine-doped zinc oxide, Appl. Phys. Lett. **97**, 122101 (2010).
[41] B. Liu, M. Gu, X. Liu, S. Huang, and C. Ni, Defect formation in chlorine-doped zinc oxide Solid State Commun. **171**, 30 (2013).
[42] A. Janotti, E. Snow, and C. G. Van de Walle, A pathway to *p*-type wide-band-gap semiconductors, Appl. Phys. Lett. **95**, 172109 (2009).
[43] I. Chatratin, I. Evangelista, B. McCandless, W. Shafarman, and A. Janotti, Defect stability in CdTe based on formation energies and migration barriers, J. Phys. Chem. C **129**, 1398 (2025).
[44] J. Buckeridge, C. R. A. Catlow, M. R. Farrow, A. J. Logsdail, D. O. Scanlon, T. W. Keal, P. Sherwood, S. M. Woodley, A. A. Sokol, and A. Walsh, Deep vs shallow nature of oxygen vacancies and consequent *n*-type carrier concentrations in transparent conducting oxides, Phys. Rev. Mater. **2**, 054604 (2018).

[45] C. Freysoldt, B. Grabowski, T. Hickel, J. Neugebauer, G. Kresse, A. Janotti, and C. G. Van de Walle, First-principles calculations for point defects in solids, Rev. Mod. Phys. **86**, 253 (2014).

[46] G. Kresse and J. Furthmüller, Efficient iterative schemes for *ab initio* total-energy calculations using a plane-wave basis set, Phys. Rev. B **54**, 11169 (1996).

[47] G. Kresse and J. Furthmüller, Efficiency of *ab-initio* total energy calculations for metals and semiconductors using a plane-wave basis set, Comput. Mater. Sci. **6**, 15 (1996).

[48] J. Heyd, G. E. Scuseria, and M. Ernzerhof, Hybrid functionals based on a screened Coulomb potential, J. Chem. Phys. **118**, 8207 (2003).

[49] P. E. Blöchl, Projector augmented-wave method, Phys. Rev. B **50**, 17953 (1994).

[50] M. Goano, F. Bertazzi, M. Penna, and E. Bellotti, Electronic structure of wurtzite ZnO: Nonlocal pseudopotential and *ab initio* calculations, J. Appl. Phys. **102**, 083709 (2007).

[51] See Supplemental Material at http://link.aps.org/supplemental/10.1103/7ts3-ktb3 for the chemical potentials used in the defect formation-energy calculations, the finite-size comparison of substitutional halogens in 96- and 192-atom supercells, and the charge states, formation energies, and FNV correction terms for the defects considered in this work.

[52] N. Ashkenov, B. N. Mbenkum, C. Bundesmann, V. Riede, M. Lorenz, D. Spemann, E. M. Kaidashev, A. Kasic, M. Schubert, M. Grundmann, *et al.*, Infrared dielectric functions and phonon modes of high-quality ZnO films, J. Appl. Phys. **93**, 126 (2003).

[53] H. Karzel, W. Potzel, M. Köfferlein, W. Schiessl, M. Steiner, U. Hiller, G. M. Kalvius, D. W. Mitchell, T. P. Das, P. Blaha, *et al.*, Lattice dynamics and hyperfine interactions in ZnO and ZnSe at high external pressures, Phys. Rev. B **53**, 11425 (1996).

[54] M. Binnewies and E. Milke, *Thermochemical Data of Elements and Compounds*, 2nd ed. (Wiley-VCH, Weinheim, Germany, 2002).

[55] V. Srikant and D. R. Clarke, On the optical band gap of zinc oxide, J. Appl. Phys. **83**, 5447 (1998).

[56] J. L. Lyons, J. B. Varley, D. Steiauf, A. Janotti, and C. G. Van de Walle, First-principles characterization of native-defect-related optical transitions in ZnO, J. Appl. Phys. **122**, 035704 (2017).

[57] Y. K. Frodason, K. M. Johansen, T. S. Bjørheim, B. G. Svensson, and A. Alkauskas, Zn vacancy as a polaronic hole trap in ZnO, Phys. Rev. B **95**, 094105 (2017).

[58] F. Oba, A. Togo, I. Tanaka, J. Paier, and G. Kresse, Zn vacancy as a polaronic hole trap in ZnO, Phys. Rev. B **77**, 245202 (2008).

[59] G. Henkelman, B. P. Uberuaga, and H. Jónsson, A climbing image nudged elastic band method for finding saddle points and minimum energy paths, J. Chem. Phys. **113**, 9901 (2000).

[60] C. Kittel and H. Kroemer, *Thermal Physics*, 2nd ed. (W. H. Freeman and Company, San Francisco, 1980).

[61] J. Lee, E. Park, N. G. Subramaniam, J. Lee, J. Lee, J. Lee, and T. Kang, Non-metallic element (chlorine) doped Zinc oxide grown by pulsed laser deposition for application in transparent electrode, Curr. Appl Phys. **12**, S80 (2012).

[62] E. Chikoidze, M. Nolan, M. Modreanu, V. Sallet, and P. Galtier, Effect of chlorine doping on electrical and optical properties of ZnO thin films, Thin. Solid. Films **516**, 8146 (2008).